ELSEVIER

Physica D 160 (2001) 127–148

PHYSICA D

www.elsevier.com/locate/physd

Modulated amplitude waves and defect formation in the one-dimensional complex Ginzburg–Landau equation

Lutz Brusch [a], Alessandro Torcini [b,c], Martin van Hecke [a,d,e], Martín G. Zimmermann [f,g], Markus Bär [a,*]

[a] *Max-Planck-Institut für Physik komplexer Systeme, Nöthnitzer Straße 38, D-01187 Dresden, Germany*
[b] *Dipartimento di Fisica, Università "La Sapienza", P.le A. Moro 2, I-00185 Rome, Italy*
[c] *Istituto Nazionale di Fisica della Materia, Unità di Firenze, Largo Enrico Fermi 2, I-50125 Firenze, Italy*
[d] *Center for Chaos and Turbulence Studies, The Niels Bohr Institute, Blegdamsvej 17, 2100 Copenhagen, Denmark*
[e] *Kamerlingh Onnes Laboratory, Leiden University, Niels Bohrweg 2, 2333 CA Leiden, The Netherlands*
[f] *Instituto Mediterráneo de Estudios Avanzados, IMEDEA (CSIC-UIB), E-07071 Palma de Mallorca, Spain*
[g] *Departamento de Física, FCEN-Universidad de Buenos Aires, Pab. I Ciudad Universitaria, 1428 Buenos Aires, Argentina*

Received 18 April 2001; received in revised form 28 September 2001; accepted 28 September 2001
Communicated by L. Kramer

Abstract

The transition from phase chaos to defect chaos in the complex Ginzburg–Landau equation (CGLE) is related to saddle-node bifurcations of modulated amplitude waves (MAWs). First, the spatial period P of MAWs is shown to be limited by a maximum P_{SN} which depends on the CGLE coefficients; MAW-like structures with period larger than P_{SN} evolve to defects. Second, slowly evolving near-MAWs with average phase gradients $\nu \approx 0$ and various periods occur naturally in phase chaotic states of the CGLE. As a measure for these periods, we study the distributions of spacings p between neighbouring peaks of the phase gradient. A systematic comparison of p and P_{SN} as a function of coefficients of the CGLE shows that defects are generated at locations where p becomes larger than P_{SN}. In other words, MAWs with period P_{SN} represent "critical nuclei" for the formation of defects in phase chaos and may trigger the transition to defect chaos. Since rare events where p becomes sufficiently large to lead to defect formation may only occur after a long transient, the coefficients where the transition to defect chaos seems to occur depend on system size and integration time. We conjecture that in the regime where the maximum period P_{SN} has diverged, phase chaos persists in the thermodynamic limit. © 2001 Published by Elsevier Science B.V.

PACS: 05.45.Jn; 03.40.Kf; 05.45.−a

Keywords: Phase chaos; Defect chaos; Complex Ginzburg–Landau equation; Coherent structures

1. Introduction

The transition from *phase* to *defect chaos* for the one-dimensional complex Ginzburg–Landau equation (CGLE) was recently related to the bifurcation properties of a family of coherent structures called modulated amplitude waves (MAWs) [1]. In this paper, the relationship between MAWs and large scale chaos is studied in detail, providing a comprehensive description of various aspects of the CGLE chaotic dynamics.

When a spatially extended system is driven sufficiently far away from equilibrium, patterns can eventually form [2,3]. In many cases, these patterns show an

* Corresponding author.
E-mail address: baer@mpipks-dresden.mpg.de (M. Bär).

0167-2789/01/$ – see front matter
PII: S0167-2789(01)00355-4

erratic behaviour in space and time: such behaviour is commonly referred to as *spatiotemporal chaos* [2–5]. Examples of extended systems displaying such chaotic dynamics in one spatial dimension include: heated wire convection [6], printers instability and film drag experiments [7], eutectic growth [8], binary convection [9], sidewall convection [10] , the far field of spiral waves in the Belousov–Zhabotinsky reaction [11], the Taylor–Dean system [12], hydrothermal [13] and internal [14] waves excited by the Marangoni effect and the oscillatory instability of a Rayleigh–Bénard convection pattern [15].

Near the pattern forming threshold, the dynamics of such systems can often be described by so-called amplitude equations. When the pattern forming bifurcation from the homogeneous state is a forward Hopf bifurcation, the appropriate amplitude equation is the CGLE [2,3], which in one spatial dimension reads as

$$\partial_t A = A + (1 + ic_1)\partial_x^2 A - (1 - ic_3)|A|^2 A, \qquad (1)$$

where c_1 and c_3 are real coefficients and the field $A = A(x, t)$ has complex values.

For different choices of the coefficients numerical investigations of the CGLE have revealed the existence of various steady and spatiotemporally chaotic states [1–5,15–26]. Many of these states appear to consist of individual structures with well defined propagation and interaction properties. It is, thus, tempting to use these structures as building blocks for a better understanding of spatiotemporal chaos. In this paper, we will essentially follow such an approach.

As a function of the coefficients c_1 and c_3, the one-dimensional CGLE (1) can exhibit two qualitatively different spatiotemporal chaotic states known as phase chaos (when the modulus $|A|$ is at any time bounded away from zero) and defect chaos (when $|A|$ can vanish leading to phase singularities). It is under dispute whether the transition from phase to defect chaos is sharp or not, and if a pure phase-chaotic, (i.e. defect-free) state can persist in the thermodynamic limit [21,27]. We will address these issues by suggesting a *mechanism* for the formation of defects related to the range of existence of MAWs.

The main points of this paper are outlined in the following and illustrated in Figs. 1 and 2. (i) Our investigation starts with the study of MAWs, which are uniformly propagating, spatially periodic solutions of the CGLE. These MAWs are parameterised by the average phase gradient ν and their spatial period P. Our study is confined to the case $\nu = 0$ for reasons specified below. Spatial profiles and the stable propagation of a particular MAW are presented in Fig. 1(a)–(c). Isolated MAW structures consisting of just one spatial period P play an important role in defect formation. In particular, for fixed CGLE coefficients the range of existence of coherent MAWs is limited by a saddle-node (SN) bifurcation which occurs when P reaches a maximal period P_{SN}. (ii) If the MAWs are driven into conditions with $P > P_{\mathrm{SN}}$ a dynamical instability occurs leading to the formation of defects (Fig. 1(d)). (iii) Slowly evolving structures reminiscent of MAWs (“near-MAWs”) are observed in the phase chaotic regime (Fig. 1(e) and (f)). In order to characterise such states, we have examined the distribution $D(p)$ of spacings p between neighbouring peaks of the phase-gradient profile. In particular, for sufficiently long spacing p, the observed phase chaos structures are often very similar to a single period of a coherent MAW (Fig. 1(f)). (iv) When a phase chaotic state displays spacings p larger than P_{SN}, phase chaos breaks down and defects are formed (e.g. at $t = 400$, $x = 360$ in Fig. 1(i)). Thus, the MAW with $P = P_{\mathrm{SN}}$ may be viewed as a “critical nucleus” for the creation of defects. In phase chaos defect formation is similar to the dynamical process by which isolated MAW structures generate defects (Fig. 1(d)). Therefore, purely phase chaotic states are those for which p remains bounded below P_{SN} (Fig. 1(g)), while defect chaos can occur when p becomes larger than P_{SN} (Fig. 1(i)). (v) A more detailed study of the probability distribution of the p shows that for large p the probability decays exponentially (Fig. 1(h) and (j)). As long as P_{SN} has a finite value, we expect that, possibly after a very long transient time, defects will be generated. (vi) However, in a finite domain of the phase chaotic region, MAWs of arbitrarily large P exist: we expect that in this region, even in the thermodynamic limit, phase chaos will persist. Fig. 2 shows the main quadrant of the CGLE coefficient space. The region of persistent phase chaos is bounded by the Benjamin–Feir–Newell

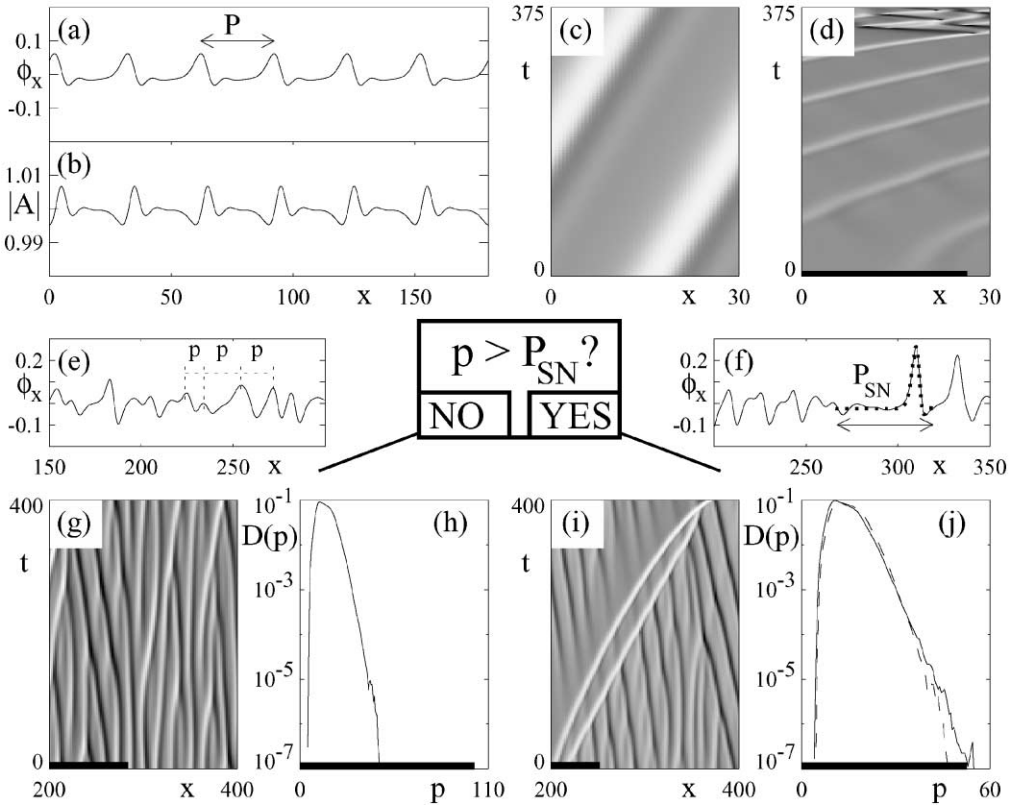

Fig. 1. Summary of our main results which constitute a picture for the formation of defects from phase chaotic states. (a and b) Example of a coherent structure: phase gradient and modulus of a period $P = 30$ MAW at $c_1 = 0.6$, $c_3 = 2$. (c) Space time plot showing the stable propagation of the MAW from (a and b) in a small system of size P with periodic boundary conditions. Subsequent space time plots also show the phase gradient encoded in grey-scale (minima appear dark, maxima bright). (d) The same MAW as initial condition creates defects at $c_1 = 0.7$, $c_3 = 2$ where $P > P_{SN} = 26.8$. Black bars above the x-axis denote the size of P_{SN} specific to the parameters of the panel. (e, g and h) Large scale chaos at $c_1 = 0.63$, $c_3 = 2$, $L = 512$. (e) Snapshot of the phase gradient profile with individual inter-peak spacings p. (g) Space time evolution of phase chaos and (h) distribution $D(p)$ showing $p \ll P_{SN}$ and no defects. A transient of $t \approx 10^4$ is not shown. (f, i and j) Large scale chaos at $c_1 = 0.65$, $c_3 = 2$, $L = 512$. (f) Snapshot of the phase gradient profile $t = 120$ before the first defect forms and the MAW (dotted, $P = P_{SN}$) overlaid onto the long structure. (i) Transient phase chaos with a fast and long structure travelling through the system which eventually nucleates defect chaos at $t = 400$, $x = 360$ (a transient of $t \approx 10^4$ is not shown). A snapshot of this structure was shown in (f). (j) The tail of the distribution of p reaches $p > P_{SN}$ due to the long structure; this leads to the break down of phase chaos. The distribution $D(p)$ shown in (h) is also reported (dashed line). From the comparison of the two it is evident that the distributions do not modify dramatically when c_1 is increased, while P_{SN} decreases noticeably.

curve (thin dot-dashed) and the curve along which $P_{SN} \to \infty$ (full curve in Fig. 2).

The outline of this paper is as follows: Section 2 is devoted to the study of the coherent MAW structures. In Section 2.2, we study the bifurcation diagram of the MAWs, starting from the homogeneous oscillation. In Section 2.3, the incoherent dynamics of near-MAW structures is presented. We show that for $p > P_{SN}$, i.e. beyond the saddle-node bifurcation, near-MAWs evolve to defects. To illustrate the origin of the saddle-node bifurcations in Section 2.4, we compare bifurcation diagrams of coherent structures for different phase gradient expansions of the CGLE. For the lowest order expansion (known as the Kuramoto–Sivashinsky equation [2]) the saddle-node bifurcation is absent while it is captured by expansions of higher order. This explains why the divergence of the phase gradient was exclusively observed

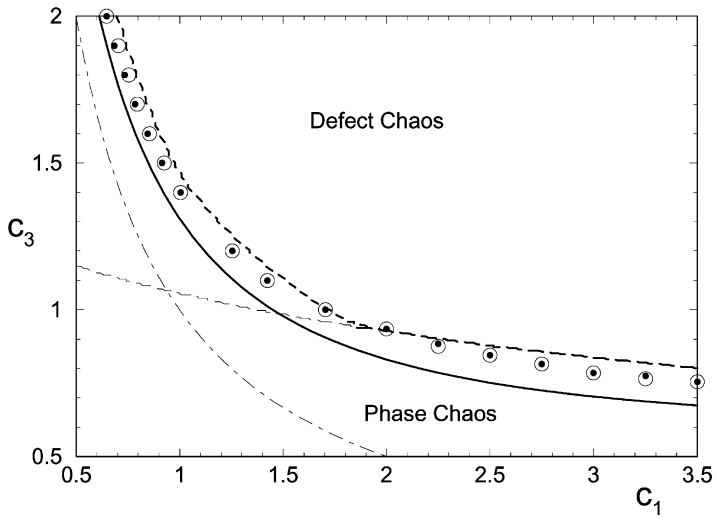

Fig. 2. Phase diagram of the CGLE, showing the Benjamin–Feir–Newell curve (thin dot-dashed) where the transition from stable homogeneous oscillations to phase chaos takes place. The curves L_1 (long dashed), L_2 (thin dashed) and L_3 (dashed) as obtained in [17,19] separate the various chaotic states. The filled circles correspond to our estimates of the L_1 and L_3 transitions based on direct simulations of the CGLE along the 17 cuts in coefficient space that we studied. The open circles correspond to the location in coefficient space where the maximal inter-peak spacing $p_{\max}$ is equal to the maximal MAW period P_{SN}. Only small discrepancies between these two can be observed. Finally, the full curve shows the $P_{\mathrm{SN}} \to \infty$ limit which we conjecture to be a lower boundary for the transition from phase to defect chaos.

in simulations [20] of higher order expansions. In Section 3, we study various aspects of spatiotemporal chaos in the CGLE, and relate the observed continuous (L_1) and discontinuous (L_3) transitions (see Fig. 2) to properties of the MAWs. *The transition to defect chaos takes place when near-MAWs with periods larger than P_{SN} occur in a phase chaotic state*. In Section 3.4, the typical values of p in the phase chaotic regime are related to the competition of two instabilities of the MAWs, and it is possible to give a good estimate for the numerically measured transition from phase to defect chaos from these considerations. A discussion of the presented results and some final remarks are reported in Section 4.

2. Modulated amplitude waves

In this section, we study the main properties of MAWs [1]. First, in Section 2.1, the coherent structure framework that we use to describe the MAWs is introduced. The bifurcation diagram of MAWs is explored in Section 2.2, with a particular focus on the saddle-node bifurcations that limit the range of existence of MAWs. In Section 2.3, we study the nonlinear evolution of near-MAWs that are "pushed" beyond their saddle-node bifurcation and show that this leads to the formation of defects. Finally, in Section 2.4, a bifurcation analysis of MAW-like coherent structures is performed in various *phase equations* that have been proposed as approximated models for the phase chaotic dynamics of the CGLE, and we show that only higher order phase equations reproduce the saddle-node bifurcation.

2.1. Coherent structures

Coherent structures in the CGLE are uniformly propagating structures of the form

$$A(x,t) = a(x - vt)\, \mathrm{e}^{\mathrm{i}\phi(x-vt)}\, \mathrm{e}^{\mathrm{i}\omega t}, \tag{2}$$

where a and ϕ are real-valued functions of $z := x - vt$. Coherent structures have been studied extensively [23–25] and play an important role in various regimes of the CGLE [16,22–25].

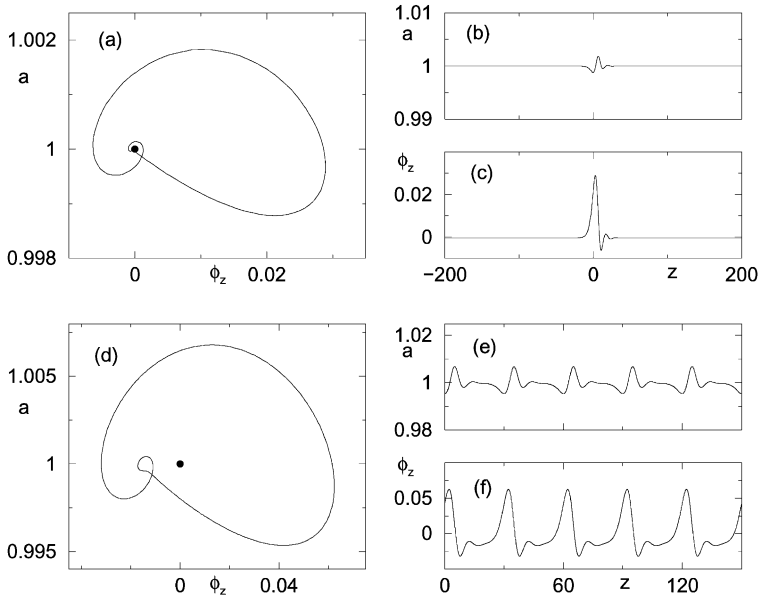

Fig. 3. Examples of ODE solutions and corresponding amplitude and phase gradient profiles of MAWs. (a) Homoclinic orbit for $c_1 = 0.55$ and $c_3 = 2$. (b and c) Corresponding profiles. (d) Periodic orbit for $c_1 = 0.60$, $c_3 = 2$ and $P = 30$. (e and f) Corresponding profiles. Dots in (a and d) denote the unstable fixed point $(1, 0, 0)$ from which these orbits emerged.

The restriction to uniformly propagating structures reduces the CGLE to a set of three coupled ordinary differential equations (ODEs). [1] These ODEs are readily found by substitution of Ansatz (2) into the CGLE (1) and read as:

$$\begin{aligned} a_z &= b, \\ b_z &= \psi^2 a - \gamma^{-1}[(1 - c_1\omega)a + v(b + c_1\psi a) \\ &\quad - (1 - c_1c_3)a^3], \\ \psi_z &= -2b\psi/a + \gamma^{-1}[c_1 + \omega + v(c_1b/a - \psi) \\ &\quad - (c_1 + c_3)a^2], \end{aligned} \tag{3}$$

where $b := a_z$, $\psi := \phi_z$, and $\gamma := 1 + c_1^2$. Solutions of the ODEs (3) correspond to coherent structures of the CGLE.

The simplest relevant solutions of these ODEs are the fixed points given by $(a, b, \psi) = (\sqrt{1 - q^2}, 0, q)$; these correspond to plane wave solutions of the CGLE where $A(x, t) = \sqrt{1 - q^2}\exp i(qx + \omega t)$ and $\omega = c_3 - q^2(c_1 + c_3)$. An example of more complex solutions of the ODEs (3) are heteroclinic orbits which correspond to coherent structures that asymptotically connect different states. Examples of such structures are fronts that connect nonlinear plane waves to the homogeneous state $A = 0$ [24] and Nozaki–Bekki holes that connect plane waves of different wave number q [24,28].

Here we present an extensive study of the structures that are associated with the *periodic orbits* of the ODEs (3). [2] These periodic orbits correspond to spatially periodic solutions of the CGLE that we have already referred to as MAWs (Fig. 3). For appropriate choices of c_1 and c_3, the period P of these MAWs can be made arbitrarily large, and in this limit the periodic orbits approach a homoclinic orbit connecting the stable and unstable manifold of one of the plane wave fixed points (Fig. 3(a)). Some of these

[1] By substituting $\kappa := a_z/a$ one reproduces the form of the ODEs used in [24] which is more appropriate for studies of fronts.

[2] For completeness, we point out that the ODEs (3) also contain complicated multi-loop orbits that correspond to more complex coherent structures which have a small basin of attraction and little relevance for the dynamics of the CGLE.

infinite period MAWs have also been referred to as "homoclinic" holes, and have been studied extensively recently [25,29]; they are qualitatively different from the well-known Nozaki–Bekki holes [28].

Even if the coefficients c_1 and c_3 are fixed, MAWs are not uniquely determined. Counting arguments, similar to those developed in [24], yield that in general we may expect a two-parameter family of solutions. Let us first perform the counting for the homoclinic orbits. As shown in [25], these orbits connect the one-dimensional unstable manifold of a fixed point with its two-dimensional stable manifold. In general, one needs to satisfy one condition to make such a connection, in other words, such a homoclinic orbit is of codimension one. Since the coherent structure Ansatz (2) has two freely adjustable parameters (ω and v), we therefore, expect a one parameter family of homoclinic orbits.

The situation for the periodic orbits of the ODEs is even simpler. Periodic orbits are of codimension zero in parameter space, and so we expect a two parameter family of periodic orbits. In other words, if we have found a periodic orbit for certain values of v and ω, then we expect this periodic orbit to persist for nearby values of the parameters v and ω.

Obviously, we can parameterise this family of coherent structures by v and ω, but this is not very insightful. Instead, we will use the following two quantities that are more directly accessible in studies of the CGLE: the spatial period P of the MAWs, and their average phase gradient $\nu := (\int_0^P \phi_x \, \mathrm{d}x)/P$. Note that for homoclinic holes, P simply goes to infinity; thus, homoclinic and periodic orbits are members of a single family.

The multiplicity of the MAWs can also be obtained by considering the instability of the plane wave solutions from which the MAWs emerge [30] (see Section 2.2). The plane waves form a one-parameter (q) family and undergo the well-known Eckhaus instability when the coefficients c_1, c_3 are increased beyond certain critical values which depend on q. In the unstable regime, a plane wave with wave number q is unstable to a whole band of perturbations with wave numbers $k \in [0, k_{\max}(q)]$ [4]. For finite systems of size L, this instability, thus, only appears when $L > L_{\min} = 2\pi/k_{\max}$. Therefore, for each q there is a unique one-parameter (L) family of perturbations that can render the plane wave unstable and at each of the corresponding bifurcations a new MAW solution emerges. Hence also by this line of reasoning MAWs form a two-parameter family.

2.2. Bifurcation scenario for MAWs

The general counting arguments given in the previous section do not provide information on the range of existence of MAWs as a function of the coefficients c_1 and c_3 and the parameters ν and P. Here we will focus our analysis on the $\nu = 0$ case since this is most relevant for the transition to defect chaos;[3] the $\nu \neq 0$ case will be treated elsewhere [31].

All bifurcation computations have been performed with the aid of the software package AUTO94 [32]. AUTO94 can trace MAW solutions through parameter space, and when it detects bifurcations it can follow the newly emerging branches. AUTO94 discretises the ODEs (3) on a periodic domain of length L, and L will play the role of the period P of the MAWs. Control of the average phase gradient $\nu = \nu_0$ is implemented via the integral constraint $\int_0^L \psi \, \mathrm{d}z = L\nu_0$. Since periodic boundary conditions result in translational invariance, we introduce an additional "pinning" condition $a_z(0) = 0$ in order to obtain unique solutions.

Under these conditions, the continuation procedure works as follows. First of all, ν and P are set to fixed values, and throughout this paper we will set $\nu = 0$. Starting from a known solution such as a plane wave or a coherent structure obtained by other means, AUTO94 is set up to trace the MAWs along trajectories in c_1, c_3 space, while calculating the parameters ω and v of these MAWs.

[3] The maximal "conserved" (during time evolution) average phase gradient vanishes approaching the transition to defect chaos [22,23]. This result is rigorous only on scales of the system size but for smaller portions ν can fluctuate around 0. Typically, we observe quasi-coherent structures (near-MAWs) in the phase chaotic regime with associate ν-values in the interval $[-0.01, +0.01]$. MAWs with such small ν do not deviate much from the $\nu = 0$ MAWs [31], therefore, the comparison of the observed structures with the $\nu = 0$ MAWs is satisfactory.

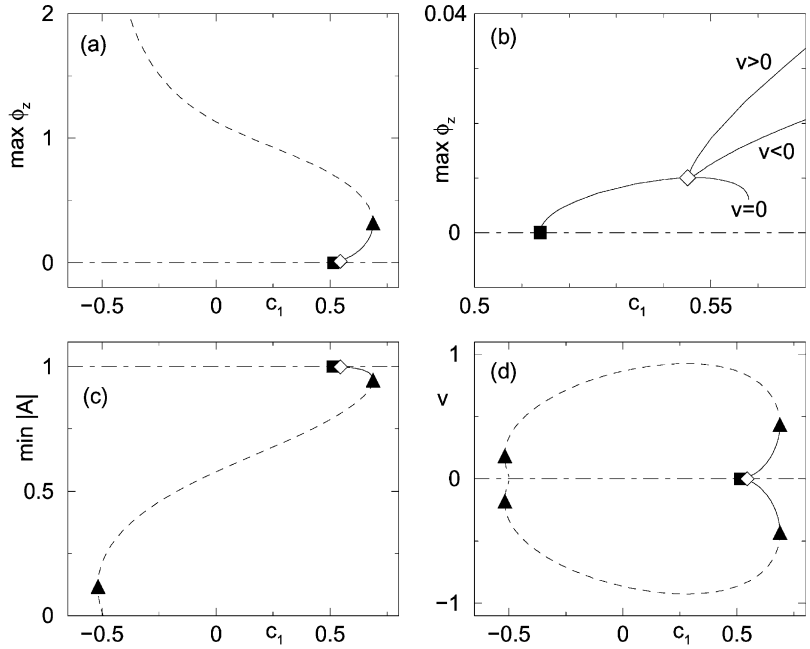

Fig. 4. Bifurcation diagrams for fixed $c_3 = 2$ and $P = 30$, showing Hopf (filled square), drift pitchfork (open diamond) and saddle-node (triangle) bifurcations. The dot-dashed line represents the homogeneously oscillating solution of the CGLE, while lower and upper branch MAWs are represented by full and dashed curves, respectively. (a) Overview of the maximum phase gradient of the MAWs as function of c_1, (b) close-up, (c) the minimum of $|A|$, and (d) the velocity v. For details see text.

The results of our bifurcation analysis are summarised in Fig. 4. When c_1 or c_3 is increased, the uniformly oscillating state of the CGLE ($A(x,t) = e^{ic_3 t}$) becomes unstable via a Hopf bifurcation, from which stationary MAWs emerge (Section 2.2.1). These stationary, left–right symmetric solutions undergo a drift pitchfork bifurcation, which leads to left and right travelling MAWs (Section 2.2.2, see also Fig. 4(b)); as discussed later, these are the solutions relevant for the dynamics in the phase chaotic regime. Following these branches of travelling MAWs, we encounter a saddle-node bifurcation where an "upper" and "lower" branch of MAWs merge (Section 2.2.3, see also Fig. 5); this bifurcation limits the range of

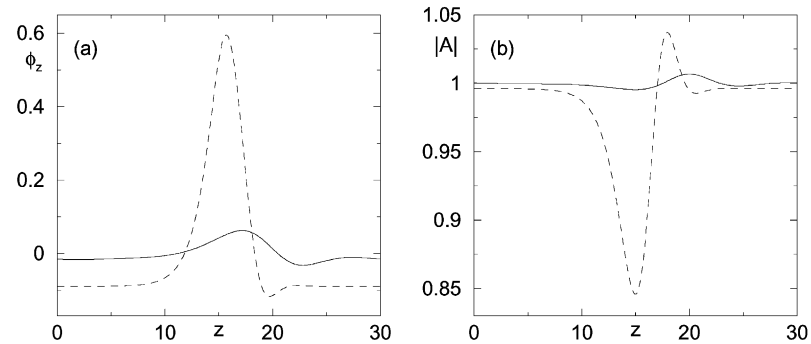

Fig. 5. (a) Phase gradient, and (b) amplitude profiles of a lower branch (full curve) and upper branch (dashed curve) MAW, obtained for $c_1 = 0.6$, $c_3 = 2$, $P = 30$.

existence of MAWs and is closely related to the formation of defects. The upper branch MAWs can be continued back to negative values of c_1, where they terminate in a solution consisting of a periodic array of shocks and stationary Nozaki–Bekki holes [28]. Upper branch MAWs with $P \to \infty$ have been studied under the name homoclinic holes [25,29].

It should be noted that, without loss of generality, we focus here on solutions with $v > 0$, for which the main peak of the phase gradient profile is positive (see Fig. 5). Solutions with $v < 0$ can be obtained from right moving MAWs by applying the mapping $x \to -x, z \to -z, v \to -v, a_z \to -a_z, \phi_z \to -\phi_z$.

2.2.1. Benjamin–Feir instability—Hopf bifurcation

Since the average phase gradient ν is conserved across bifurcations, we start the continuation procedure from the uniformly oscillating solution $A(x,t) = \mathrm{e}^{\mathrm{i}c_3 t}$ that has $\nu = 0$. On an infinite domain this uniformly oscillating solution becomes unstable via the so-called Benjamin–Feir instability when $c_1 c_3 \geq 1$ [3]. In a finite domain of size L, the onset of this instability is shifted to higher values of the product $c_1 c_3$;[4] this finite size effect is relevant for our studies since the spatial period $L = P$ is fixed in the continuation procedure.

In the ODEs (3), the fixed point $(a, b, \psi) = (1, 0, 0)$ corresponds to the homogeneously oscillating solution. For given values of the period P, this fixed point undergoes a Hopf bifurcation at values of c_1 and c_3 where in the CGLE (1) the mode with wave number $2\pi/P$ becomes unstable (see footnote 4). This Hopf bifurcation was analytically shown to be supercritical for sufficiently small ν and large P in earlier studies [15,30]; our numerical results are consistent with this. For finite P, the solution bifurcating from the fixed point is a periodic orbit which approaches a homoclinic orbit in the limit $P \to \infty$. The solutions of the CGLE that correspond to these orbits are stationary, reflection symmetric MAWs; an example of these is shown in Fig. 9(a).

2.2.2. Drift pitchfork bifurcation

When the CGLE coefficients c_1 and/or c_3 are increased further, the stationary MAW undergoes a drift pitchfork bifurcation [33] from which two new branches of asymmetric ($v \neq 0$) MAWs emerge (see Fig. 4(b)); one of these moves to the left, one to the right. The locations of both the Hopf and the drift pitchfork bifurcation approach the Benjamin–Feir–Newell curve for large P (Fig. 6(a)), while for smaller P the drift pitchfork occurs for increasingly larger coefficients c_1 and c_3. However, only when these coefficient lie in the range shown as the shaded area in Fig. 6(b), the pitchfork bifurcation can occur. Otherwise, only stationary MAWs are found. For increasing c_1 and c_3 these MAWs become pulse-like and finally approach the solitonic solutions of the nonlinear Schrödinger equation [24] (Fig. 6(c) and (d)).

For the case $\nu \neq 0$ [31], the initial plane wave already breaks the reflection symmetry, the initial MAW has nonzero velocity and the drift pitchfork bifurcation is replaced by its typical unfolding [34].

2.2.3. Saddle-node bifurcation

Along the branch of right travelling MAWs that we described above, the maximum of the phase gradient grows with increasing c_1 and c_3 until a SN bifurcation is reached, where these MAWs merge with another branch of MAW-like solutions. To distinguish these branches we refer to them as the "lower" and the "upper" branch; e.g. see Figs. 4 and 8. The lower branch MAWs are the key to understand more of the phenomenology of phase chaos. The upper branch MAWs can, similarly to the lower branch MAWs, be parameterised by ν and P, but for the same parame-

[4] The linear stability analysis of the uniformly oscillating solutions $A_0(x,t) = \mathrm{e}^{\mathrm{i}c_3 t}$, can be performed by considering the following perturbed solution $A(x,t) = (1 + a(x,t))\,\mathrm{e}^{\mathrm{i}c_3 t}$ [4]. Where $a(x,t) = \sum_k a_k\,\mathrm{e}^{\mathrm{i}kx+\lambda_k t}$ with $\lambda_k = \sigma_k + i\Omega_k$. It is straightforward to show that the real part of the growth-rate σ_k is, up to fourth order in k, given by

$$\sigma_k \sim -(1 - c_1 c_3)k^2 - \tfrac{1}{2}(1 + c_3^2)c_1^2 k^4.$$

From this expression it is clear that $\sigma_k > 0$ only if $c_1 c_3 > 1$ (this is nothing else than the Newell criterion). Moreover, there exists a critical value $k_0^2 = [2(c_1 c_3 - 1)]/[c_1^2(1 + c_3^2)]$ above which σ_k is always negative. For finite size systems, the smallest allowed wave vector is $k_{\min} = 2\pi/L$, therefore, the uniform oscillation becomes unstable for $k_{\min} \leq k_0$ and this condition allows to derive the corresponding critical values of the parameters c_1 and c_3.

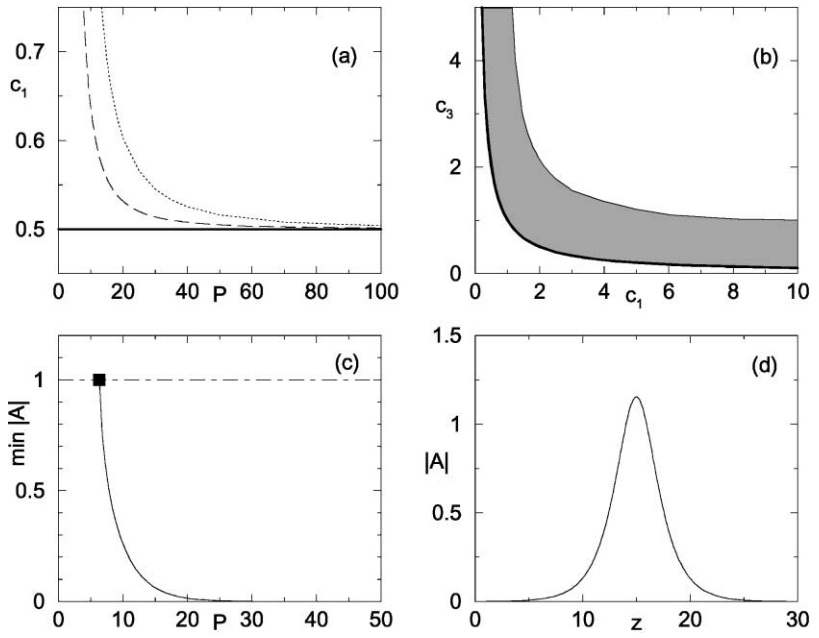

Fig. 6. (a) Location of Hopf (dashed curve) and drift pitchfork bifurcation (dotted curve) in c_1, P space for $c_3 = 2.0$. (b) The shaded area reported in the c_1, c_3 coefficient space indicates where the drift pitchfork bifurcation does occur. The thick full curve in (a and b) indicates the Benjamin–Feir–Newell instability for infinite domains. (c) Example of a bifurcation diagram for large values of the coefficients $c_1 = 10$, $c_3 = 5$ where the drift pitchfork bifurcation does not occur. For increasing P the MAW solutions approach regular arrays of stationary pulses; an example of such a pulse is shown in (d) for $P = 30$.

ters, they present more pronounced modulations (see Fig. 5).

The most important aspect of the saddle-node bifurcation is that it limits the range of existence of MAWs, since we will show that this limit is responsible for the transition from phase to defect chaos. Fixing $\nu = 0$, the locations of these bifurcations form a two-dimensional manifold in the three-dimensional space spanned by c_1, c_3 and P. In Fig. 7(a) the saddle-node curves are shown in the c_1, c_3 coefficient plane for a number of fixed periods P; for larger P, the values of c_1, c_3 where the bifurcation takes place decrease. In Fig. 7(b) the saddle-node curves for a number of fixed values of c_3 are shown in the P,

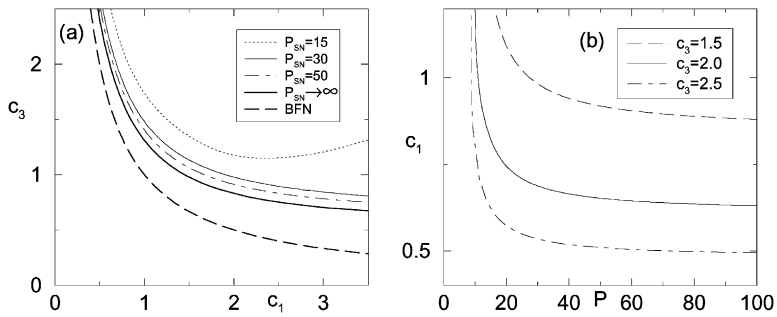

Fig. 7. Locations of the saddle-node bifurcations in the c_1, c_3 plane (a) and the P, c_1 plane (b). BFN denotes the Benjamin–Feir–Newell curve.

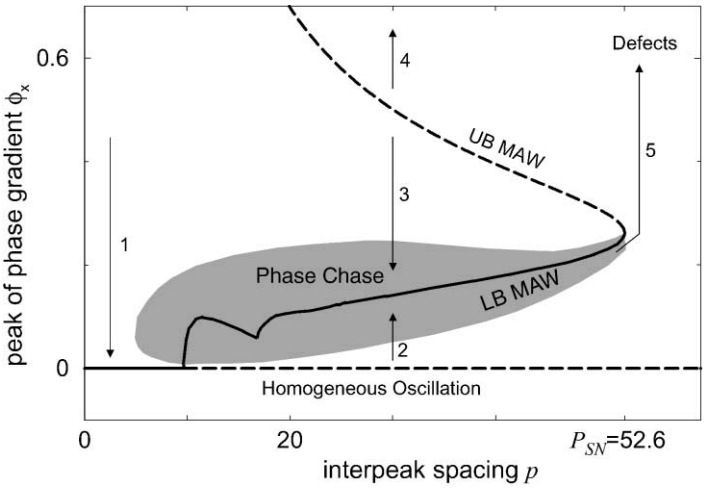

Fig. 8. Illustration of the relation between MAW structures and phase chaos for $c_1 = 0.65$, $c_3 = 2$. Both for MAWs and for an extended profile obtained from a phase chaotic state one can extract the values of subsequent phase gradient peaks (vertical axis) and their inter-peak spacing (horizontal axis). The curves show the bifurcation diagram for the lower branch (LB) MAWs and upper branch (UB) MAWs while the shaded area indicates the typical values for near-MAW structures that occur in phase chaos. Full (dashed) curves denote stable (unstable) solutions for system size $L = p$. Arrows show the typical evolutions of near-MAWs. The coefficients here are equal to those in Fig. 1(f), (i) and (j) and for this case we have found that phase chaos is only a long lived transient: the shaded area reaches P_{SN} just before defects appear.

c_1 plane; for larger c_3 (c_1), the saddle-node occurs for smaller values of P and c_1 (c_3).[5] Once the coefficients c_1 and c_3 are fixed, we define P_{SN} as the period for which the saddle-node bifurcation occurs. Note that there is also a range of coefficients c_1 and c_3 (between the $P \to \infty$ and $c_1 c_3 = 1$ curve where the saddle-node bifurcation does *not* occur.

2.3. Evolution of perturbed MAWs

In this section, we will show that many basic aspects of the phenomenology of the CGLE can be understood from a typical bifurcation diagram of MAWs such as shown in Fig. 8. We have chosen fixed coefficients $c_1 = 0.65$ and $c_3 = 2$ and varied the spatial period P of MAWs that exist at these coefficients. Three families of solutions are represented: the homogeneous oscillation, the lower branch (LB) and the upper branch (UB) MAWs. The shaded area schematically indicates the near-MAW structures observed in phase chaotic states such as shown in Fig. 1(f), (i) and (j). The arrows in Fig. 8 represent the dynamical evolution of perturbed MAWs, and their direction can be obtained by performing a linear stability analysis.

Linear stability: As discussed in Section 2.2, the homogeneous solution is stable against short wavelength perturbations (arrow 1), and turns unstable via the Hopf bifurcation that also generates the lower branch MAWs (arrows 2). As discussed in [25,29], upper branch MAWs have at least one unstable eigenvalue, and the dynamical evolution of perturbations is directed away from upper branch MAWs (arrows 3 and 4).

The linear stability of lower branch MAWs will be discussed in more detail in Section 3.4. It turns out that perturbations of lower branch MAWs can evolve in many ways, but in almost all cases the ensuing dynamics remains close to the lower MAW branch (shaded area in Fig. 8). The only exception we have found to this rule is when a MAW is pushed beyond the saddle-node bifurcation (arrow 5).

Nonlinear evolution: Here we want to go beyond the linear analysis and study the nonlinear evolution

[5] An exception on this rule occurs for large c_1, where the dependence of c_3 on P at the saddle-node becomes non-monotonic.

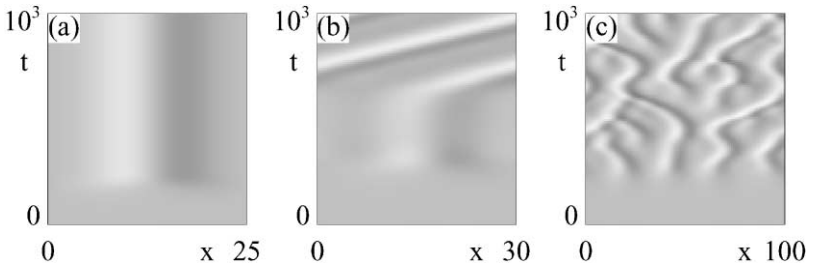

Fig. 9. The evolution of an unstable homogeneous state towards lower branch MAW dynamics, for $c_1 = 3$ and $c_3 = 0.6$. The coefficients c_1 and c_3 are chosen such that no saddle-node bifurcation occurs for any P. (a) Evolution towards a stable stationary lower branch MAW for system size $L = 25$ and (b) towards a stable drifting lower branch MAW for system size $L = 30$. Note that for the coefficients chosen, the drift pitchfork bifurcation occurs at $P = 27.7$. (c) Evolution towards phase chaos for system size $L = 100$. Incoherent evolution of structures characterised by local concentrations of phase gradients can be clearly observed. We think of these structures as "near" MAWs.

of MAWs along the arrows of Fig. 8. The examples (at different choices of the coefficients) of the dynamics shown here are not exhaustive, but should serve to illustrate typical behaviour which appears to be very robust.

Arrow 2: When the uniform oscillation becomes linearly unstable perturbations grow. To the left of the saddle-node, perturbations evolve to dynamics dominated by lower branch MAWs (Fig. 9). For small system sizes, stable MAWs may occur (Fig. 9(a) and (b)), while for larger systems periodic sequences of MAWs are unstable with respect to the so-called *interaction* or *splitting* instabilities [1,35] that will be discussed in Section 3.4. Hence a perturbed unstable homogeneous state typically does not converge to a train of coherent MAWs, but instead evolves to phase chaos (Fig. 9(c)). In the context of the bifurcation diagram, note that the disordered structures observed in the phase chaotic evolution are quite similar to lower branch MAWs. The shaded area in Fig. 8 represents this "near-MAW" behaviour.

Arrows 3 and 4: Upper branch MAWs are always unstable due to the positive eigenvalue associated with the saddle-node bifurcation. The resulting incoherent dynamics has been studied quite extensively in the context of hole-defect dynamics [25,29]. (i) When a perturbation has pushed an upper branch MAW towards the "lower" part of the bifurcation diagram, the structure decays towards lower branch MAWs (arrow 3). An example of a space time plot for the decay towards a lower branch MAW is shown in Fig. 10(a). (ii) When the perturbation pushes the MAW towards the "upper" side of the diagram, the phase gradient peak that characterises MAWs grows without bound, and at

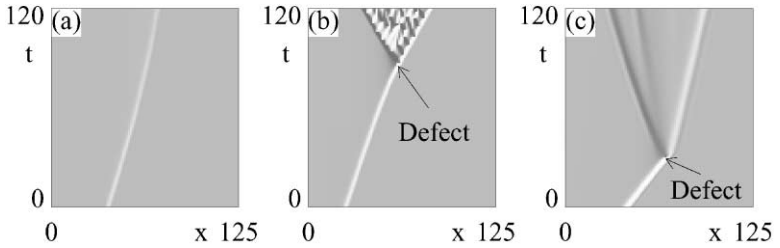

Fig. 10. Evolution of perturbations of the upper branch MAWs. The coefficients c_1 and c_3 are chosen such that no saddle-node bifurcation occurs for any value of P. (a) A slowing down and spreading of the phase gradient characterises the decay to a lower branch MAW for $c_1 = 0.55$ and $c_3 = 2$. (b) For the same coefficients, another perturbation leads to an increase in velocity and divergence of the phase gradient. A defect occurs, from which hole-defect dynamics spreads for these coefficients. (c) For $c_1 = 3$ and $c_3 = 0.6$ a perturbed upper branch MAW leads to a defect, but defects do not percolate through the system.

the same time the minimum of $|A|$ approaches zero: a defect is formed (arrow 4). The dynamics *after* such a defect has formed depends on the values of the coefficients c_1 and c_3. Two different examples are shown in Fig. 10(b) and (c). For more details, see Section 3.

Arrow 5: So far we have encountered two scenarios: if the phase gradient peak of a structure is "larger" than that of an upper branch MAW, then it will grow out to form defects. If it is "smaller", it will decay back in the direction of the lower branch MAWs. The latter process frequently occurs in phase chaos, preventing the formation of defects, while the former process needs to be initiated by appropriate initial conditions. However, when the upper and lower branches approach each other and disappear in a saddle-node bifurcation, there are no structures left to prevent arbitrary small perturbations to grow out to defects. This dynamical process, which is represented by arrow 5 in Fig. 8, is the core of our argument: defect formation takes place beyond the saddle-node bifurcation.

2.4. Breakdown of phase description

An alternative approach to describe the creation of defects from phase chaotic states is via blow-ups in so-called phase-equations [20]. Phase equations are based on the observation that close to the onset of phase chaos (near the Benjamin–Feir–Newell curve) the amplitude is "slaved" to the phase dynamics. In this situation a phase equation can be obtained by a gradient expansion [4]. The expansion including all parity-symmetric terms up to fourth order [20] reads

$$\begin{aligned}\frac{\partial\phi}{\partial t} &= \Omega_2^{(1)}\frac{\partial^2\phi}{\partial x^2} + \Omega_2^{(2)}\left(\frac{\partial\phi}{\partial x}\right)^2 + \Omega_4^{(1)}\frac{\partial^4\phi}{\partial x^4} \\ &\quad + \Omega_4^{(2)}\frac{\partial\phi}{\partial x}\frac{\partial^3\phi}{\partial x^3} + \Omega_4^{(3)}\left(\frac{\partial^2\phi}{\partial x^2}\right)^2 \\ &\quad + \Omega_4^{(4)}\left(\frac{\partial\phi}{\partial x}\right)^2\frac{\partial^2\phi}{\partial x^2} \qquad (4)\end{aligned}$$

where $\Omega_2^{(1)} = 1 - c_1c_3$, $\Omega_2^{(2)} = -(c_1 + c_3)$, $\Omega_4^{(1)} = -c_1^2(1+c_3^2)/2$, $\Omega_4^{(2)} = -2c_1(1+c_3^2)$, $\Omega_4^{(3)} = -c_1(1+c_3^2)$, $\Omega_4^{(4)} = -2(1 + c_3^2)$. The lowest order description of phase chaos is obtained when the parameters $\Omega_4^{(2)}$, $\Omega_4^{(3)}$ and $\Omega_4^{(4)}$ are set equal to zero; the resulting equation is known as the Kuramoto–Sivashinsky equation [2].

The phase equations with higher order terms included have been studied via direct integration by Sakaguchi [20]. For the full Eq. (4), Sakaguchi observed finite time divergences of the phase gradient for coefficients close to the transition from phase to defect chaos in the CGLE. He attributed such divergences to the occurrence of defects in the CGLE. No blow-up of the phase gradient is observed for Eq. (4) without the last term, or for the simple Kuramoto–Sivashinsky equation. Recently, Abel et al. [36] quantified the increasing discrepancies between the phase equations of different orders and the full dynamics in the CGLE with increasing distance from the Benjamin–Feir–Newell curve and identified the relative importance of the various terms in Eq. (4).

Since the essential ingredient of our theory is the occurrence of a saddle-node bifurcation, we have investigated the bifurcation scenario for various truncations of the phase Eq. (4). In the context of phase dynamics, our Ansatz (2) becomes of the form

$$\phi(x,t) = \tilde{\phi}(x - vt) + (\omega - c_3)t. \qquad (5)$$

We have studied MAW-like structures occurring in the phase equations by employing the same methodology as for the CGLE; the average phase gradient value ν is fixed to 0 and P parameterises the spatial period of the MAW. In Fig. 11, we compare bifurcation diagrams and MAW profiles for different expansions at the parameters $c_1 = 3.5$, $P = 50$.

For all phase equations considered here, the coherent structures are again born in a Hopf and undergo a drift pitchfork bifurcation, beyond which the maximal phase gradients increase. This leads to increasing discrepancies between different approximations. In particular, the coherent structures for Eq. (4) exhibit saddle-node bifurcations at parameter values not far from those for corresponding MAWs in the CGLE; nevertheless the MAWs of Eq. (4) deviate substantially from the CGLE MAWs for the upper branch of MAWs. The Kuramoto–Sivashinsky equation, and Eq. (4) without the last term, do not exhibit a saddle-node bifurcation. Since these latter two

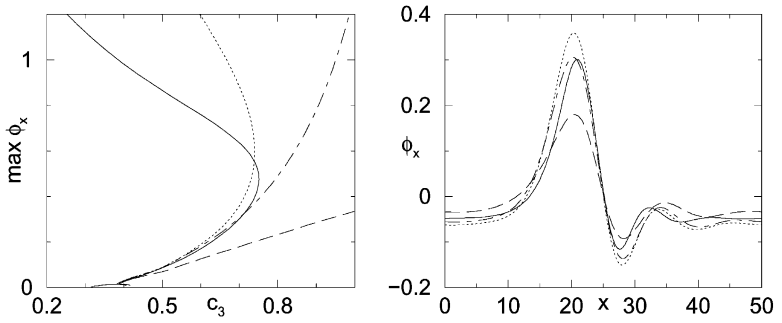

Fig. 11. Comparison of different phase expansions: Eq. (4) (dotted), Eq. (4) without the last term (dot-dashed), Kuramoto–Sivashinsky equation (dashed) and CGLE (full curve). Parameters are $c_1 = 3.5$, $\nu = 0$, $P = 50$. (a) Bifurcation diagrams, and (b) spatial profiles of lower branch coherent structures at $c_3 = 0.7$.

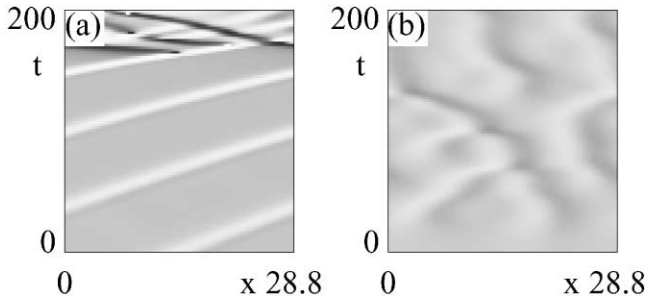

Fig. 12. Defect formation at $c_3 = 2$, $c_1 = 0.7$. (a) Defect formation. As initial condition we took a lower branch MAW with $P < P_{SN} = 26.8$ which we embedded in a background of zero wave number. The system size L here is equal to 28.8, which is larger than P_{SN} and a defect is formed; for $L < P_{SN}$ this defect formation does not take place. (b) Random initial conditions in general evolve to MAW like structures with $P < P_{SN}$ which do not lead to defects; the "critical" nucleus that leads to defect formation has a rather small basin of attraction here.

models do not experience blow-up, we can safely conclude that these observations confirm our picture, and that the saddle-node bifurcations of coherent structures play the same crucial role in both the full CGLE and its phase equations.

3. Large scale chaos

In this section, we will study the dynamical evolution of the CGLE near the transitions from phase to defect chaos. The transition between these two states can either be hysteretic or continuous: in the former case, the transition is referred to as L_3, in the latter as L_1.[6]

[6] Another relevant line that appears in the parameter plane is the so-called L_2-line which is the transition from defect to phase chaos in the hysteretic regime.

How are defects generated from phase chaos? Let us start to consider a *small* system in which a stable lower branch MAWs has been created. When we fix the coefficients c_1 and c_3 and steadily increase the size of the system, and hence the period P of the MAW, we find that as soon as we push P beyond P_{SN}, the MAW structure blows up to form defects. An example of this is shown in Fig. 12(a). In a similar fashion, defects are created when the system size L is fixed, and either c_1 or c_3 are increased until $P_{SN} < L$ (Fig. 1(c) and (d)).

How is this related to phase chaos? As shown in Fig. 12(b), typical phase chaotic states show much more incoherent dynamics, containing many MAW like structures but of much smaller period. Our central conjecture is therefore, that the transitions from phase to defect chaos are triggered by the occurrence of near-MAW structures in a phase chaotic state with $\nu = 0$ (See footnote 3) and periods larger than P_{SN},

the spatial period of the critical nucleus for defect creation.

To test this conjecture, we have numerically investigated the distribution of inter-peak spacings p of the phase gradient profile (see Fig. 1(e) and (f)). In Section 3.1, we discuss the definition of p and the details of our numerical analysis. In particular, we have examined in the c_1, c_3 plane 17 different "cuts" across the L_1 and L_3 transition lines. In Section 3.2, the results of our numerics along a cut through the L_1 transition line are presented, while Section 3.3 is devoted to the L_3 transition. We will show that the presence of inter-peak spacings p larger than P_{SN} accurately predicts the transition from phase to defect chaos (Fig. 2). In the last Section 3.4, we will show that a reasonable, parameter-free estimate of the numerically observed transitions can be obtained via a linear stability analysis of the MAWs.

3.1. Identification of MAWs in the phase-chaotic regime

To verify our main conjecture, we have to characterise the MAW structures occurring in the phase-chaotic regime. In general this is a complicated task, since the phase gradient profile of a typical phase chaotic state (see Fig. 1(e) and (f) and Fig. 13) consists of many peaks of different size, spacing and shape; a priori it is unclear how to compare these to MAW profiles. However, a close inspection of the defect forming process reveals that while closely spaced phase gradient peaks evolve in a quite erratic way, well spaced peaks appear to have a more regular dynamics and frequently their overall shape resembles that of MAWs (see Fig. 13). These large period near-MAWs modify their shape quite slowly with respect to the other structures present in the chaotic field, and propagate over a disordered background. Therefore, we study the distribution of inter-peak distances p, keeping in mind that the tail of this distribution is relevant for defect generation.

The phase gradient profile of a coherent MAW (see Fig. 1(a) and Fig. 5(a)) shows a secondary maximum. To obtain the correct period P of a near-MAW, such small extrema should be neglected when the inter-peak

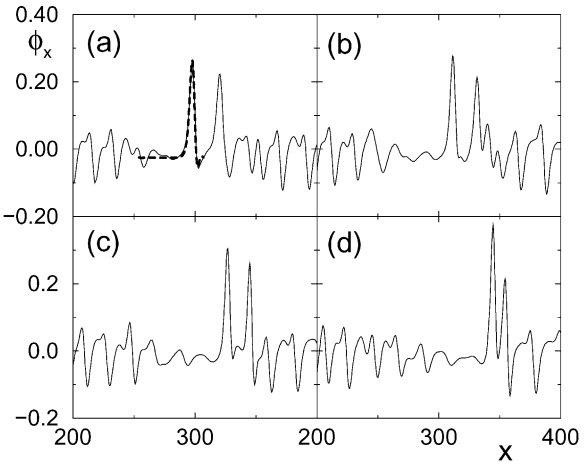

Fig. 13. Local phase gradient of the chaotic field just before defect formation for $c_1 = 0.65$ and $c_3 = 2$. Panel (a) is a snapshot of the field at a time $t = 120$ before the occurrence of the defect, (b–d) are successive snapshots taken at time intervals $\delta t = 30$. In (a) also the shape of the MAW at the saddle-node is superimposed (thick dashed line) on the profile.

spacing p is measured. We introduce a cut-off for the size of the phase gradient peak equal to the size of the secondary extremum of the MAW with the largest P. As an additional result of this cut-off, small fluctuations are not considered as MAW peaks. It should be noted that the tail of the distribution of p is rather insensitive to the precise value of this cut-off.

In order to estimate the probability density $D(p)$, for every time interval $\tau = 0.5$, the inter-peak periods p of the spatial profile of the phase gradient are determined. In addition, for every snapshot the largest value $p_{\max}$ of the inter-peak spacing p is stored separately, and this leads to the distribution $D(p_{\max})$. From the spatial profile of $|A|$ the distribution $D(|A|)$ and the minimal amplitude value $|A|_{\min}$ can be derived. This latter quantity is used to detect defects: when $|A|_{\min}$ falls below a value of 0.1, we take this as an indication of a defect.

Extensive simulations have been made possible thanks to an innovative time-splitting code which ensures precision and stability comparable with pseudo-spectral codes, but is noticeably faster [23]. The spatial resolution Δx has been set to 0.5 and the integration time step to 0.05. Simulations have been carried out for integration times ranging from

$t = 5 \times 10^5$ to 3×10^7 and for a typical system size $L = 512$; occasionally, runs have been performed with $L = 100$, 200 and 5000. Typically, our runs start from random initial conditions of the type $A_k(t = 0) = |A|_k(t = 0)\, \mathrm{e}^{\mathrm{i}\phi_k(t=0)}$ (where $A_k(t) = A(k\Delta x, t)$ and $\phi_k(t) = \phi(k\Delta x, t)$) with

$$|A|_k(0) = 1 + r_k \tag{6}$$

$$\phi_k(0) = \phi_{k-1}(0)0.8 + q_k \tag{7}$$

where r_k and q_k are random numbers uniformly distributed in $[-0.05, +0.05]$ and $\phi_1(0) = 0.0005$. This initial condition (7) leads to a smooth phase and the formation of defects due to initial discontinuities is avoided.

In Sections 3.2 and 3.3, we will consider in detail two particular cuts in the (c_1, c_3) coefficient space, one across the L_1 and one across the L_3 curve. In particular, we will analyse the behaviour of the probability densities $D(|A|)$, $D(p)$ and $D(p_{\max})$ for both transitions.

3.2. L_1 transition

In this section, we concentrate on the L_1 transition that is observed when the value of c_1 is fixed at 3.0 and c_3 is varied.

Transition to defect chaos: Starting from random initial conditions we have integrated the dynamics of the CGLE for long durations. For a fixed system size L we observe that, as a function of the total integration time, the value of c_3^* for which defects are formed appears to decrease. Similar behaviour occurs when the system size L is increased for fixed integration times. For example, for an integration time of 3×10^7 and $c_1 = 3$ we find for system size 100, 200 and 512 critical values 0.82, 0.81 and 0.79, respectively. For a size $L = 5000$ and integration times 3×10^6 a critical value of 0.79 is also found.

Note that even the lowest value of c_3^* for the numerically measured transition obtained here is far above the lower bound $c_3^\infty = 0.704$ which is the value of c_3 where the size of the critical nucleus for defect formation diverges ($P_{\mathrm{SN}} \to \infty$). Below, we will give an estimate of the critical value $\hat{c}_3$ for which the defect density should vanish in the thermodynamic limit by extrapolating finite time and finite size data.

Distribution of p: Let us now consider the distribution of p for various coefficients c_3 near the L_1 transition. It is clear from the data reported in Fig. 14 that the shape of these distributions is quite insensitive to the presence or absence of defects. This can be partly explained by the fact that just above the L_1 transition defects arise in the system as rare isolated events occurring during the spatio-temporal evolution, as shown in Fig. 10(c). This is fully consistent with earlier observations that the L_1 transition is continuous [17,19,21]. We focus on the tail of the probability density $D(p)$, since this gives information on the probability to observe defects. Our numerical results suggest an exponential decay, i.e. $D(p) \propto \exp(-\alpha p)$ with $\alpha = 0.6$ for sufficiently large p.

Similarly to the apparent transition value c_3^*, the values associated to extremal events $|A|_{\min}$ and $p_{\max}$ depend on integration times and system sizes. By assuming that $D(p)$ remains finite (but likely exponentially small) for large p, we can expect that for long enough times, rare events associated with large values p will occur, and hence, defects can form after possibly very long transients.

Crossover behaviour: A good order parameter to identify the occurrence of the transition starting from the defect chaos phase near the L_1 transition is the *defect density* δ_D which measures the number of defects occurring per space and time unity. In the defect chaos regime $\delta_D > 0$, while it vanishes at the L_1-transition. Now we can relate this order parameter to the tail of the distribution of p. Our conjecture states that defects should arise when $p > P_{\mathrm{SN}}$, therefore, the defect density δ_D should be related to the probability to have structures of period $p > P_{\mathrm{SN}}$, i.e.

$$\delta_D \propto \int_{P_{\mathrm{SN}}}^{\infty} \mathrm{d}p D(p) \propto \mathrm{e}^{-\alpha P_{\mathrm{SN}}}; \tag{8}$$

where $D(p) \propto \exp(-\alpha p)$ has been used. If we now assume that the distribution $D(p)$ does not vary significantly across the transition (as is evident from Fig. 14), then the change in the probability to have $p > P_{\mathrm{SN}}$ is dominated by the changes in P_{SN} with c_3. A reasonable fit of our bifurcation data for P_{SN} (see Fig. 7) in

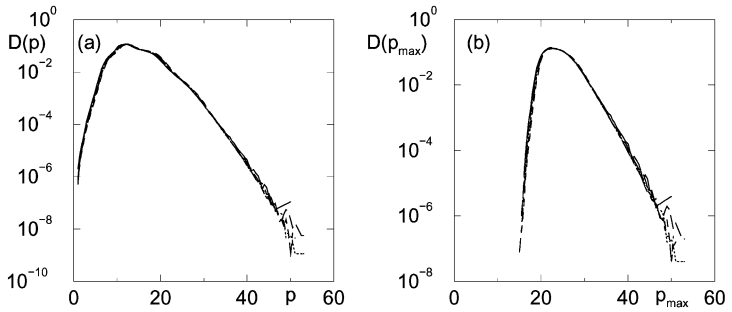

Fig. 14. Probability densities (a) $D(p)$ and (b) $D(p_{\max})$ for $c_1 = 3$ and various values of c_3 on a lin-log scale. The curves refer to c_3 below $c_3^* = 0.79$ (namely to $c_3 = 0.77$ and 0.78), as well as to values corresponding to the defect chaotic regime: $c_3 = 0.79$, 0.80 and 0.81. The system size was $L = 512$ and the integration times where $t = 5 \times 10^5$ for $c_3 = 0.81$, $t = 5 \times 10^6$ for $c_3 = 0.80$ and $t = 25 \times 10^6$ for all other values.

the interval $30 \leq P_{\mathrm{SN}} < 300$ is

$$P_{\mathrm{SN}} \approx \frac{\beta}{c_3 - c_3^{\infty}}, \tag{9}$$

where $\beta \approx 4.38$. Combining this result with the Ansatz (8), we immediately obtain the following expression for the defect density:

$$\delta_D \propto \mathrm{e}^{-\alpha\beta/(c_3 - c_3^{\infty})}. \tag{10}$$

A similar expression was proposed in [17,21] for the defect density near the L_1 transition.

In order to verify if the expression (10) is reasonable also for our choice of the parameters, we have estimated the probability [23]

$$w(|\hat{A}|) = \int_0^{|\hat{A}|} d|A| D(|A|), \tag{11}$$

to observe an amplitude less than $|\hat{A}|$. This quantity gives a more precise characterisation of the L_1-transition than δ_D, because it measures not only the extreme events corresponding to true defects, but also the tendency of the system to generate structures characterised by small $|A|_{\min}$. We estimated the quantity (11) for several $|\hat{A}|$ values and for various c_3 parameter values in the defect chaos regime. Reporting $\ln[w(|\hat{A}|)]$ as a function of $1/(c_3 - \hat{c}_3)$ a reasonable linear scaling is observed in the range $0.795 \leq c_3 \leq 0.85$, for $0.1 \leq |\hat{A}| \leq 0.5$, with the choice $\hat{c}_3 = 0.72$. The value $\hat{c}_3$ where the defect density should asymptotically vanish is much smaller than c_3^* obtained via direct numerical simulations but still bigger than $c_3^{\infty} = 0.704$ where $P_{\mathrm{SN}} \to \infty$.

We can now easily estimate the integration time needed to observe a tiny shift of the apparent value c_3^* towards the corresponding asymptotic value $c_3^{\infty} \approx 0.704$. Limiting our analysis to system size $L = 512$, a typical time-scale to observe a defect at $c_3 = 0.79$ is $t \sim 3 \times 10^7$. At this value of c_3, $P_{\mathrm{SN}} = 46.5$, while for $c_3 = 0.739$, $P_{\mathrm{SN}} = 105$. Invoking the exponential decay of $D(p)$, one immediately finds that the time scale to observe a defect at $c_3 = 0.739$ is of order 10^{17}, which is completely outside the reach of present day computers.

3.3. L_3 transition

In order to characterise the L_3 transition from phase to defect chaos in more detail $c_3 = 2$ has been fixed, while the coefficient c_1 is varied. The L_3 transition is hysteretic [17,19]: to the left of L_3 one may have phase or defect chaos depending on the initial conditions. Beyond the L_3 phase chaos breaks down and defects occur spontaneously for any initial condition. In order to study the dynamics across this transition we, therefore, initialised the simulations with initial conditions (6) and (7) or used relaxed phase chaos configurations corresponding to values of c_1 far below the L_3 line.

The probability densities $D(p)$ and $D(p_{\max})$ are shown in Fig. 15. For $c_1 < c_1^* = 0.65$ all distributions collapse on a unique curve, but as soon as defects arise the distributions change substantially. Whenever

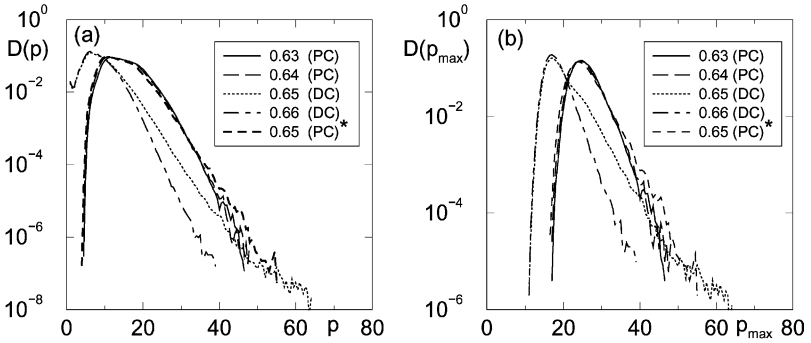

Fig. 15. Probability densities (a) $D(p)$ and (b) $D(p_{\max})$ for $c_3 = 2$ and various values of c_1 reported in a lin-log scale. The data are for a system size $L = 512$ and for integration times ranging from $t = 5 \times 10^5$ for $c_1 = 0.63$, 0.64, 0.66 and 0.65 (PC)* to $t = 2.5 \times 10^6$ for $c_1 = 0.65$ (DC). The labels DC and PC indicate that we are in presence or absence of defects, respectively. The label (PC)* refers to the regime before defect formation at $c_1 = 0.65$.

a defect is generated, hole-defect dynamics takes place (see Fig. 10(b)). As a result phase chaos is replaced by defect chaos. The noticeable modification of the distributions, thus, reflects the fact that the L_3 transition is discontinuous. Also the probability density for $|A|$ changes abruptly across the L_3 transition.

3.4. Mechanism for the selection of p

When approaching the transition to defect chaos from the Benjamin–Feir–Newell curve, three parameter regions, corresponding to different dynamical regimes, can be distinguished (Fig. 18). The first encountered region corresponds to infinite values of P_{SN}: here we expect no defects to occur, irrespectively of system size and integration time. The phase chaos is the asymptotic regime in this first region. Then, when c_1 and/or c_3 are increased, a crossover regime is reached where extreme events (large inter-peak spacings) may lead to defect formation. Here phase chaos can persist as a long lived transient, but eventually we expect it to break down. Then, when c_1 and/or c_3 are even further increased, we experience a dramatic drop in transient times, and defect chaos sets in quite rapidly. We understand this drop to occur when typical values of p (and not rare extreme events) become larger than the corresponding P_{SN} values.

An approximate prediction for the location of the apparent phase to defect chaos transition (numerically obtained from the defect density) can be achieved in terms of a simple linear stability analysis of the MAWs (Figs. 16 and 17). A key element in our framework is the "typical large value" of p as a function of coefficients c_1 and c_3; here we will identify two linear instabilities that act to either increase or decrease p, and their balance sets a scale for typical p that will predict the location of the transition from phase to defect chaos rather well.

Due to translational and phase symmetries both MAW branches have neutral modes, i.e. Goldstone modes. The eigenvalue associated with the saddle-node bifurcation is positive for MAWs of the upper branch and negative for the lower branch. In what follows the lower branch MAWs are considered exclusively.

Splitting: The spatial structure of a MAW of large period consists, roughly, of a homogeneous plane wave part and a local peak part. For the parameter regime we consider here, fully extended plane waves are linearly unstable, and so we may expect that the MAW spectrum will be dominated by this instability for sufficiently large values of P. Our linear stability analysis indeed shows that for appropriate parameters ($L = P$) and small enough P, all eigenvalues $\lambda_i < 0$, but when we increase P, MAWs become linearly unstable ($\lambda_{\mathrm{split}} > 0$, Fig. 16). The shape of the unstable eigenmodes (Fig. 16(b)) suggests that this instability leads to the growth of a new peak in the homogeneous part of the MAW, and this is indeed the behaviour observed in numerical simulations of the perturbed MAW (Fig. 16(c) and (d)). As a result two (or more)

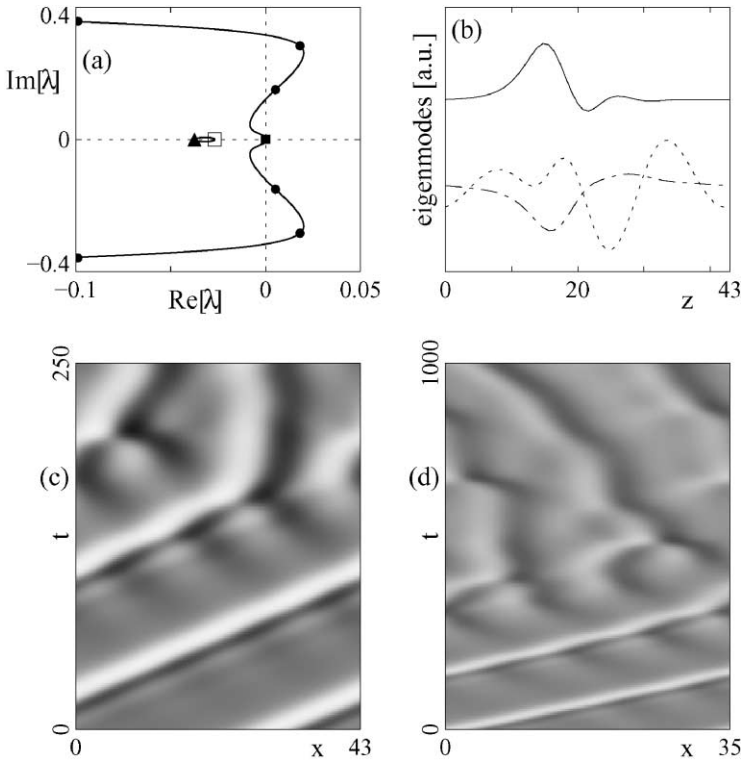

Fig. 16. Results of the linear stability analysis: (a) leading part of the eigenvalue spectrum (continuous spectrum denoted by the full curve, Goldstone modes by a filled square, saddle-node by filled triangle, interaction by open square and splitting modes in $L = P$ by dots, respectively). (b) Splitting eigenmodes (dot-dashed and dotted, $\lambda_{\text{split}} = 0.018 \pm 0.28i$) of the phase in $L = P$ compared with spatial MAW profile of the phase gradient (full curve). (c and d) Space time plots showing the splitting of a MAW initially perturbed by small noise. Parameters are $c_1 = 3$, $c_3 = 0.72$, $P = 43$ near L_1 for (a–c) and $c_1 = 0.65$, $c_3 = 2$, $P = 35$ near L_3 for (d).

short MAWs with smaller P will appear. We interpret this process as the *splitting* of a MAW in two or more smaller MAWs and we call the eigenmodes associated to such instability "splitting modes".

Clearly, this instability tends to reduce the peak-to-peak distances p and prevents MAWs to cross the SN boundary; in the phase chaotic regime this instability *tends to inhibit defect generation*.

Interaction: By using a Bloch Ansatz [37], we extended the stability analysis to systems with n identical pulses ($L = nP$). For $n > 1$, an additional instability may appear [38] (see Fig. 17). Eigenvalues $\lambda_{\text{int}} > 0$ are found mainly for small P (typically $P < 30$). The shape of the eigenmodes, i.e. an alternating sequence of positive and negative translational Goldstone modes (Fig. 17(b)), suggests that the instability is due to the *interaction* between adjacent MAWs. This interaction shifts adjacent peaks into opposite directions, thereby creating occasional larger values of p (Fig. 17(c) and (d)). In phase chaos this process leads to an increase of the spacing p between some peaks, thus *enhancing the generation of defects*.

Competition of instabilities: Both the splitting and interaction mechanisms are similar to instabilities observed in the Kuramoto–Sivashinsky equation [4,35]. We believe that phase chaos is governed by the competition of these two mechanisms that tend to increase or decrease the inter-peak spacings p. Almost independent of the coefficients the splitting instability dominates for MAWs with $P > 30$. This can explain why large inter-peak spacings $p > 30$ become rare as reported in Figs. 14 and 15.

We suggest a connection between the interchanging dominance of these two different instabilities and the

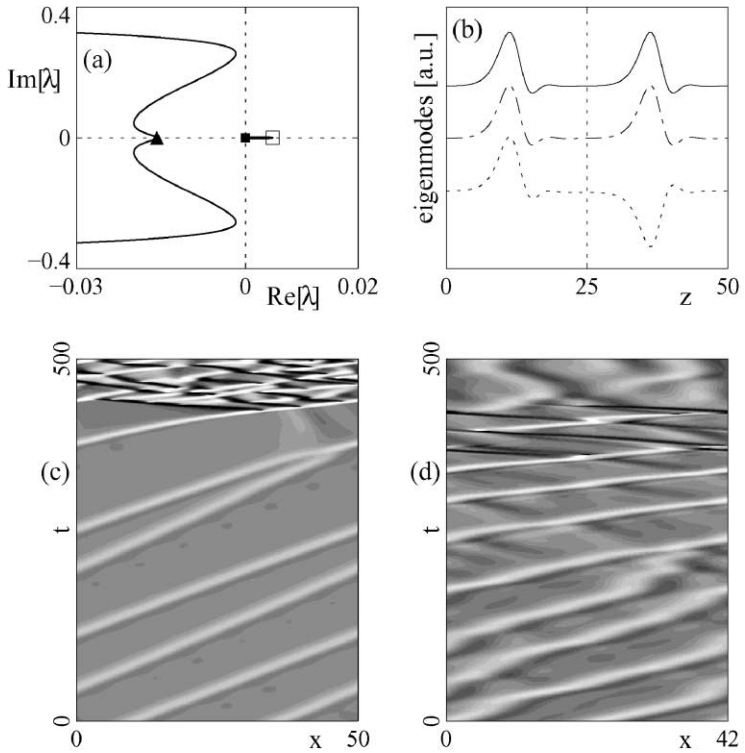

Fig. 17. Results of the linear stability analysis: (a) leading part of the eigenvalue spectrum (continuous spectrum denoted by the full curve, Goldstone modes by a filled square, saddle-node by filled triangle and interaction by open square at $\lambda_{\text{int}} = +0.0048$, respectively), (b) Goldstone mode (dot-dashed) and interaction eigenmode (dotted curve) for the phase compared with spatial MAW profile of the phase gradient (full curve) in $L = 2P$. (c and d) Space time plots showing the attraction of two periods of the same MAW initially perturbed by the interaction eigenmode. Parameters are $c_1 = 0.7$, $c_3 = 2$, $P = 25$ near L_3 for (a–c) and $c_1 = 3$, $c_3 = 0.85$, $P = 21$ near L_1 for (d).

sudden change of δ_D (near L_1) or the transient times before defect occurrence (near L_3). We calculated the linear stability spectra for a variety of coefficients and periods P close to P_{SN}. From these we obtain a curve in coefficient space (Fig. 18) where the real parts of interaction and splitting eigenvalues are *equal*. For larger c_1 or c_3, P_{SN} occurs in the range where interaction and defect formation dominate, while for smaller c_1 and c_3, splitting dominates and defect formation becomes rare.

As shown in Fig. 18, the curve where the two instabilities are equally strong near the saddle-node bifurcation gives a rather good estimate of where the apparent transition from phase to defect chaos occurs. Notice that in this "balance of instabilities" picture, there is no tunable parameter: once we have calculated P_{SN} and the instabilities of the MAWs for a range of coefficients, a precise prediction for the "transition" from phase to defect chaos can be given.

4. Discussion and final remarks

In this section, we report some open questions related to defect formation, together with some final remarks and a brief outlook.

Further refinements: In order to accurately test our results, we have measured for each of the 17 cuts and for several values of the coefficients across the L_1- or L_3-lines the amplitude distribution $D(|A|)$ and the phase gradient peak-to-peak spacing distribution $D(p)$. We conjectured that defects occur if and only if $p > P_{\text{SN}}$. Indeed, we observe that in 11 out of 17 points such conjecture is fulfilled. On the remaining

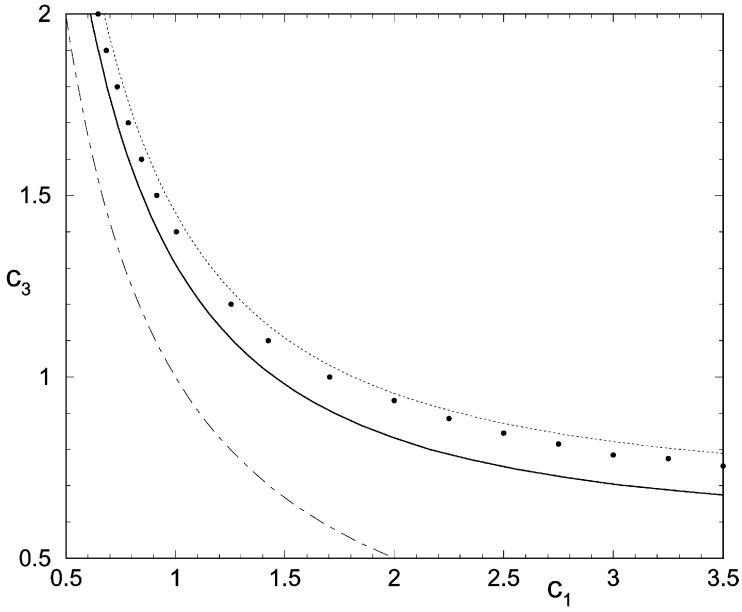

Fig. 18. Space of (c_1, c_3)-coefficients for the CGLE with the Benjamin–Feir–Newell curve (dot-dashed), the lower bound $P_{SN} \to \infty$ (full) and the stability-based estimate (dotted) for the transition from phase to defect chaos. The symbols refer to our numerical data for the appearance of defects.

six points the theoretical conjecture leads to an estimation of the transition lines within a maximal error bar of 3%.The points determined following the conjecture are indicated as empty circles in Fig. 2. The small deviations may have different reasons, that we summarise below:

(i) If fluctuations occurring during the phase chaotic dynamics are only moderate, such as happens near the L_3 transition line or for small system sizes, more complex coherent structures can survive for a short time. Here we analysed only the shortest coherent structures characterised by a single hump. We believe that this is sufficient to understand the main aspects of the dynamics of large systems. However, longer combined MAWs with more than one hump emerge from periodic MAWs via period doubling bifurcations. The existence of the long combined MAWs is limited by saddle-node bifurcations analogously to single MAWs, but these bifurcations occur at slightly bigger values of the parameters c_1 and c_3. Therefore, the appearance of these more complicated structures can delay defect formation even if one inter-peak spacing within the structure is bigger than P_{SN} of the single MAW.

(ii) Near the L_1 line the dynamical fluctuations in the phase chaotic regime are stronger than in the proximity of the L_3 line. In this case and for sufficiently high values of the parameter c_1 we observed situations where not only the structure with the longest inter-peak spacing but also the neighbouring structures were involved in the defect formation.

(iii) The assumption to consider MAWs with $\nu = 0$ is only an approximation. If the average phase gradient locally (on scales P) deviates from 0 then the saddle-node bifurcation slightly shifts towards smaller coefficients [31].

As far as the numerically obtained L_1 and L_3 lines are concerned, we observe that both these lines lie to the left of the ones determined in earlier numerical studies [19]. This is due to the fact that our simulations are of longer duration then those performed previously. This confirms the expecta-

tion that such transition lines will shift towards the Benjamin–Feir–Newell curve for increasing system size and integration times [21]. Moreover, some authors claim that indeed in the thermodynamic limit L_1 and L_3 will coincide with the Benjamin–Feir–Newell curve and the phase chaos regime will disappear [27]. On the basis of our simulations we cannot exclude such a possibility for higher space dimensions, but based on the results presented in this paper we conjecture that the saddle-node line for $P \to \infty$ provides a lower boundary for the transition from phase to defect chaos in the one-dimensional CGLE.

Final remarks: We have presented a systematic study of MAWs in the CGLE. These periodic coherent structures originate from supercritical bifurcations from the homogeneous oscillation of the CGLE due to the Benjamin–Feir instability. The range of existence of MAWs is bounded by saddle-node bifurcations occurring for values of c_1 and c_3 that depend on the period P of the MAWs. Approaching the transition from phase to defect chaos, near-MAWs with large P occur in phase chaos, and defects are generated when the period of these near-MAWs becomes larger than the spatial period P_{SN} of the critical nucleus. This scenario is valid for both the L_1 and L_3 transition. The divergence of P_{SN} for coefficients in the phase-chaos regime led us to conjecture that there is a lower bound for the transition from phase to defect chaos. Considerations of the linear stability properties of MAWs in light of their tendency to increase or decrease the typical period p in phase chaos, has led us to a fit-free estimate of the apparent transition from phase to defect chaos that fits the numerical data well.

Altogether, our study leaves little space for doubt that the transition from phase chaos to defect chaos in the CGLE is governed by coherent structures and their bifurcations. From a general viewpoint, our analysis shows that there is no collective behaviour that drives the transition. Instead, strictly local fluctuations drive local structures beyond their saddle-node bifurcation and create defects.

Outlook: We want to stress here that the extension of the analysis to MAWs with nonzero average phase gradients [31], will be of considerable interest for experimentalists, because in some recent experiments concerning Rayleigh–Bénard or Marangoni convection in quasi-one-dimensional geometries, supercritical Eckhaus instabilities of plane wave trains and the corresponding emergence of stable saturated MAWs have been observed [13–15]. These states are analogous to what happens for the 1d CGLE when phase chaotic solutions with $\nu \neq 0$ are considered [22,23].

The relevance of MAWs for two-dimensional structures is suggested by recent experimental evidence of MAWs observed in connection with superspiral and spiral break-up occurring in a Belousov–Zhabotinsky reaction [11]. Moreover, in the phase chaotic regime of the 2d CGLE, the correspondence between long inter-peak spacings (here diameter of cells) and the strength of the local modulation has already been noticed numerically [27]. In the 2d CGLE defects carry a topological charge and are created in pairs. This will significantly change the late stage of defect formation and additional mechanisms present in 2d remain to be explored. Thereby it might turn out that phase chaos exists in the thermodynamic limit in 1d only but not in 2d as previously conjectured [27].

Acknowledgements

It is a pleasure to acknowledge discussions with H. Chaté, M. Howard and L. Kramer. A.T. and M.B. are grateful to ISI Torino for providing a pleasant working environment during the Workshop on “Complexity and Chaos” in October 1999. A.T. was partially supported by the MURST-COFIN00 grant “Chaos and localisation in classical and quantum mechanics” and would also like to thank Caterina, Daniel, Katharina and Sara for providing him with a faithful representation of a chaotic evolution. M.G.Z. is supported from a post-doctoral grant of the MEC (Spain) and FOMEC-UBA (Argentina). M.v.H. acknowledges financial support from the EU under contract ERBFMBICT 972554.

References

[1] L. Brusch, M.G. Zimmermann, M. van Hecke, M. Bär, A. Torcini, Phys. Rev. Lett. 85 (2000) 86.

[2] Y. Kuramoto, Chemical Oscillations, Waves and Turbulence, Springer, Berlin, 1984.
[3] M.C. Cross, P.C. Hohenberg, Rev. Mod. Phys. 65 (1993) 851.
[4] P. Manneville, Dissipative Structures and Weak Turbulence, Academic Press, San Diego, 1990;
T. Bohr, M.H. Jensen, G. Paladin, A. Vulpiani, Dynamical Systems Approach to Turbulence, Cambridge University Press, Cambridge, 1998.
[5] I.S. Aranson, L. Kramer, The world of complex Ginzburg–Landau equation, Rev. Mod. Phys., in press.
[6] J.M. Vince, M. Dubois, Physica D 102 (1997) 93.
[7] M. Rabaud, S. Michalland, Y. Couder, Phys. Rev. Lett. 64 (1990) 184;
D.P. Vallette, G. Jacobs, J.P. Gollub, Phys. Rev. E 55 (1997) 4274.
[8] S. Akamatsu, G. Faivre, Phys. Rev. E 58 (1998) 3302.
[9] M. Lücke, W. Barten, M. Kamps, Physica D 61 (1992) 183.
[10] Y. Liu, R.E. Ecke, Phys. Rev. Lett. 78 (1997) 4391.
[11] Q. Ouyang, J.M. Flesselles, Nature 379 (1996) 143;
Q. Ouyang, H.L. Swinney, G. Li, Phys. Rev. Lett. 84 (2000) 1047;
L.Q. Zhou, Q. Ouyang, Phys. Rev. Lett. 85 (2000) 1650.
[12] P. Bot, I. Mutabazi, Eur. Phys. J. B13 (2000) 141.
[13] N. Mukolobwiez, A. Chiffaudel, F. Daviaud, Phys. Rev. Lett. 80 (1998) 4661;
J. Burguete, H. Chaté, F. Daviaud, N. Mukolobwiez, Phys. Rev. Lett. 82 (1999) 3252.
[14] A. Wierschem, H. Linde, M.G. Velarde, Phys. Rev. E 62 (2000) 6522.
[15] B. Janiaud, A. Pumir, D. Bensimon, V. Croquette, H. Richter, L. Kramer, Physica D 55 (1992) 269.
[16] A. Pumir, B.I. Shraiman, W. van Saarloos, P.C. Hohenberg, H. Chaté, M. Holen, in: C.D. Andereck, F. Hayot (Eds.), Ordered and Turbulent Patterns in Taylor–Couette Flow, Plenum Press, New York, 1992, p. 173.
[17] B.I. Shraiman, A. Pumir, W. van Saarloos, P.C. Hohenberg, H. Chaté, M. Holen, Physica D 57 (1992) 241.
[18] M.V. Bazhenov, M.I. Rabinovich, A.L. Fabrikant, Phys. Lett. A 163 (1994) 87.
[19] H. Chaté, Nonlinearity 7 (1994) 185;
P.E. Cladis, Palffy-Muhoray (Eds.), Spatio-Temporal Pattern Formation in Nonequilibrium Complex Systems, Addison Wesley, Reading, 1995, p. 33.
[20] H. Sakaguchi, Prog. Theor. Phys. 84 (1990) 792.
[21] D.A. Egolf, H.S. Greenside, Phys. Rev. Lett. 74 (1995) 1751.
[22] R. Montagne, E. Hernández-García, M. San Miguel, Phys. Rev. Lett. 77 (1996) 267;
R. Montagne, E. Hernández-García, A. Amengual, M. San Miguel, Phys. Rev. E 55 (1997) 151.
[23] A. Torcini, Phys. Rev. Lett. 77 (1996) 1047;
A. Torcini, H. Frauenkron, P. Grassberger, Phys. Rev. E 55 (1997) 5073.
[24] W. van Saarloos, P.C. Hohenberg, Physica D 56 (1992) 303; W. van Saarloos, P.C. Hohenberg, Physica D 69 (1993) 209 [Errata].
[25] M. van Hecke, Phys. Rev. Lett. 80 (1998) 1896.
[26] G. Giacomelli, R. Hegger, A. Politi, M. Vassalli, Phys. Rev. Lett. 85 (2000) 3616.
[27] P. Manneville, H. Chaté, Physica D 96 (1996) 30.
[28] K. Nozaki, N. Bekki, J. Phys. Soc. Jpn. 53 (1984) 1581.
[29] M. van Hecke, M. Howard, Phys. Rev. Lett. 86 (2001) 2018.
[30] G. Hager, Quasiperiodische Lösungen der eindimensionalen komplexen Ginzburg–Landau Gleichung, Diploma Thesis, University of Bayreuth, Germany, 1996.
[31] L. Brusch, A. Torcini, M. Bär, Physica D, submitted for publication.
[32] E.J. Doedel, X.J. Wang, T.F. Fairgrieve, AUTO94: Software for continuation and bifurcation problems in ordinary differential equations, Applied Mathematics Report, California Institute of Technology, 1994.
[33] M. Kness, L. Tuckerman, D. Barkley, Phys. Rev. A 46 (1992) 5054.
[34] G. Iooss, D.D. Joseph, Elementary Stability and Bifurcation Theory, Springer, Berlin, 1980 (Chapter 3).
[35] H.-C. Chang, E.A. Demekhin, E. Kalaidin, SIAM J. Appl. Math. 58 (1998) 1246;
H.-C. Chang, E.A. Demekhin, D.I. Kopelevich, Physica D 63 (1993) 299.
[36] M. Abel, H. Chaté, H. Voss, in preparation.
[37] N.W. Ashcroft, N.D. Mermin, Solid State Physics, Holt, Rinehart and Winston, New York, 1976.;
P. Collet, J.-P. Eckmann, Instabilities and Fronts in Extended Systems, Princeton University Press, 1990.
[38] M. Or-Guil, I.G. Kevrekidis, M. Bär, Physica D 135 (2000) 154.